Supplementary Information: New insight into tuning magnetic phases of RMn$_6$Sn$_6$ kagome metals

S. X. M. Riberolles[1,2], Tianxiong Han[1,2], Tyler J. Slade[1,2], J. M. Wilde[1,2], A. Sapkota[1,2], Wei Tian[3], Qiang Zhang[3], D. L. Abernathy[3], L. D. Sanjeewa[4,5], S. L. Bud'ko[1,2], P. C. Canfield[1,2], R. J. McQueeney[1,2*], B. G. Ueland[1,2*]

[1*]Division of Materials Sciences and Engineering, Ames National Laboratory, U.S. DOE, Iowa State University, Ames, 50010, IA, USA.
[2]Department of Physics and Astronomy, Iowa State University, Ames, 50010, IA, USA.
[3]Neutron Scattering Division, Oak Ridge National Laboratory, Oak Ridge, 37831, TN, USA.
[4]University of Missouri Research Reactor, University of Missouri, Columbia, 65211, MO, USA.
[5]Department of Chemistry, University of Missouri, Columbia, 65211, MO, USA.

*Corresponding author(s). E-mail(s): mcqueeney@ameslab.gov; bgueland@ameslab.gov;

1 Supplementary Discussion

1.1 Additional Single-Crystal Neutron Diffraction Data

Supplementary Figure 1 displays the temperature evolution of the magnetic diffraction along $(0,0,l)$ and $(1,0,l)$ to complement Fig. 2 of the main text. The nuclear component of the intensity is significantly weaker for $(1,0,0)$ than for $(0,0,2)$, and the transition at T_{spiral} is more clearly seen in the $(1,0,l)$ data.

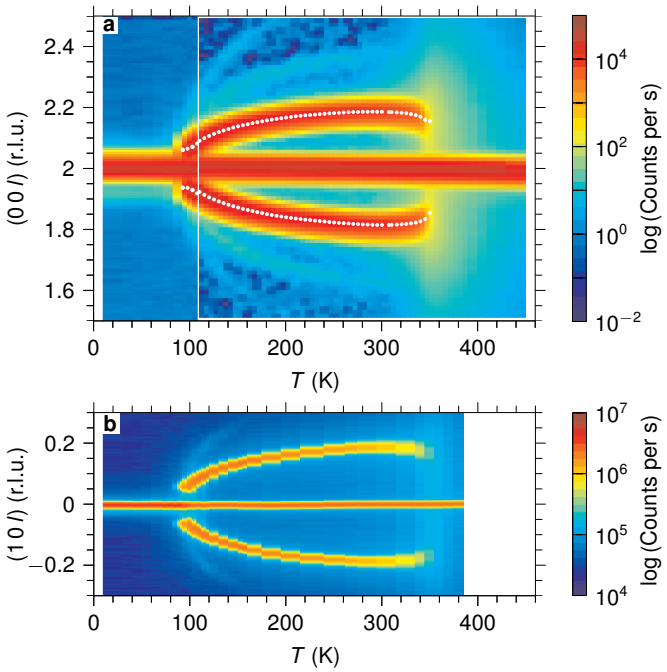

Supplementary Figure 1 Temperature evolution of the neutron-diffraction intensity for $ErMn_6Sn_6$ from single-crystal neutron diffraction measurements along the **a** $(0, 0, l)$ and **b** $(1, 0, l)$ reciprocal-lattice directions. The $(1, 0, l)$ data were measured during one experiment, whereas the $(0, 0, l)$ data were taken over two experiments.

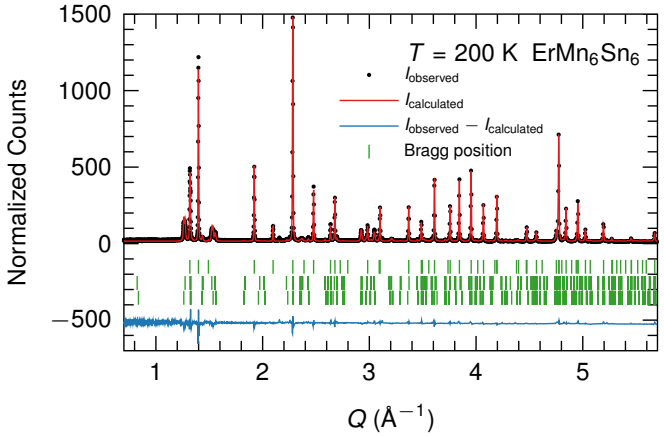

Supplementary Figure 2 Neutron powder diffraction data for $ErMn_6Sn_6$ collected at $T = 200$ K. The red curve through the data points shows the fit from a Rietveld refinement using triple-spiral magnetic order and the bottom blue curve shows the difference between the data and fit. Vertical tick marks indicate Bragg peak positions. The top set of ticks is for the structural-Bragg peaks. The bottom two sets are for magnetic-Bragg peaks.

Supplementary Table 1 Parameters from Rietveld refinements of neutron powder diffraction data for $ErMn_6Sn_6$ taken at $T = 200$ K. The superscript N indicates a parameter for the structural phase whereas the + and − superscripts indicate parameters for the two magnetic phases described in the text. The avg superscript indicates the average value for the two magnetic phases. Ordered magnetic moments μ_{Er} and μ_{Mn} for Er and Mn, respectively, are given in units of μ_B, δ is given in degrees, and τ is given in reciprocal-lattice units of $2\pi/c$.

μ^{-}_{Er}	μ^{-}_{Mn}	δ^{-}	τ^{-}	μ^{+}_{Er}	μ^{+}_{Mn}	δ^{+}	τ^{+}
4.8(2)	1.8(1)	14.3(2)	0.1789(4)	3.1(2)	2.2(1)	13.7(2)	0.1963(4)

μ^{avg}_{Er}	μ^{avg}_{Mn}	δ^{avg}	τ^{avg}	R^{N}_{Bragg}	R^{-}_{Bragg}	R^{+}_{Bragg}
3.9(3)	2.0(1)	14.0(2)	0.1876(6)	5.36	16.4	12.3

1.2 Neutron Powder Diffraction

Supplementary Figure 2 shows the neutron powder diffraction pattern for $T = 200$ K. Rietveld refinements were made using one phase to describe the chemical structure and two phases to describe the triple-spiral magnetic structure. Two magnetic phases were used because, as described in the main text, the lineshapes of the magnetic-Bragg peaks are split. For 200 K, two gaussian peaks and a background can be used to describe the lineshape. The most straightforward way to model the data for the Rietveld refinements is to assume two equally populated domains, each corresponding to one of the slightly different values of $\boldsymbol{\tau} = (0, 0, \tau^{\pm})$. Thus, each magnetic phase corresponds to either τ^{+} or τ^{-} and we refined the values of the ordered magnetic moments for Er (μ_{Er}) and Mn (μ_{Mn}), τ, and the angle $(\Phi-\delta)$ for each phase separately. The results are given in Table 1. The R_{Bragg} values indicate acceptable agreement between the triple-spiral model and the data. Refinements made allowing $\boldsymbol{\mu}_{Er}$ and $\boldsymbol{\mu}_{Mn}$ to have components along $\mathbf{c}$ did not yield sensible results.

1.3 Magnetic-Bragg Peak Lineshape Splitting

Supplementary Figure 3 compares $(1, 0, l)$ cuts collected in the vicinity of T_{spiral} during neutron diffraction experiments for two different single-crystal samples of $ErMn_6Sn_6$. Fits of the primary-satellites' lineshapes from our first experiment using gaussian-peak components return a difference between the centers of the gaussian components of $\Delta\tau_1 = 0.015$ at $T = 98$ K and 0.017 at 103 K. $\Delta\tau_1 = 0.016$ is obtained from our second experiment for 100 K. The close agreement of $\Delta\tau_1$ for two different samples suggests that the lineshape splitting is intrinsic to the compound, and intrinsic to a single magnetic domain, rather than arising from different domains hosting spirals with slightly different periodicity.

1.4 Estimation of Hamiltonian parameters

Exchange parameters. Fits to the spin-wave dispersions from previous inelastic-neutron-scattering (INS) data for $TbMn_6Sn_6$ (Tb166) provide a starting point for estimating the various Mn-Mn and Mn-Er isotropic exchange constants defined in the main text in Eq. (1). The values for Tb166, in meV, are; $\mathcal{J}_0^{MM} = -28.8$, $\mathcal{J}_1^{MM} = -4.4$, $\mathcal{J}_2^{MM} = -19.2$, $\mathcal{J}_3^{MM} = 1.8$, and $\mathcal{J}^{MT} = 1.8$ meV [1, 2]. Here, $\mathcal{J}_2^{MM}$ is the dominant

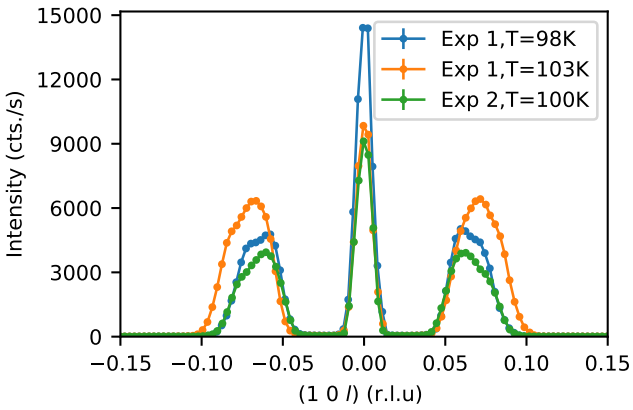

Supplementary Figure 3 $ErMn_6Sn_6$ single-crystal neutron diffraction cuts across $(1, 0, l)$ in the vicinity of T_{spiral} from our two experiments. Both samples reveal similar splittings of lineshapes the satellite magnetic-Bragg peaks.

ferromagnetic (FM) interlayer coupling. The stability of spiral or ferrimagnetic (FIM) states is then dependent on the balance of the competing $\mathcal{J}_1^{\text{MM}}$ and $\mathcal{J}_3^{\text{MM}}$ interactions, which have opposite signs. We discuss this competition in terms of the ratios $x = \mathcal{J}_1^{\text{MM}}/\mathcal{J}_2^{\text{MM}} > 0$ and $y = \mathcal{J}_3^{\text{MM}}/\mathcal{J}_2^{\text{MM}} < 0$. The Tb166 value of $x = 0.23$ is consistent with estimates based on neutron diffraction and magnetization data for Y166, so we retain this value. The Tb166 value of $y = |-0.09|$ is smaller than the value of $y = |-0.12|$ reported for Y166. The smaller of the two y values is very close to the stability range of the FIM phase and therefore can only stabilize long-period spiral order. This is not consistent with experimental data in the spiral phase for Er166, so we set y to the value reported for Y166, or $\mathcal{J}_3^{\text{MM}} = 2.3$ meV.

The Mn-R interaction, $\mathcal{J}^{MR}$, is known to be antiferromagnetic (AFM) for the heavy rare-earths and both INS data [1, 2] and density-functional-theory (DFT) calculations [3] indicate that $\mathcal{J}^{MR}$ decreases in magnitude from R = Gd $\rightarrow$ Tm. We estimate the value of $\mathcal{J}^{\text{ME}} = 1.35$ meV using INS data for Er166 and magnetization data, as described below. This value is lower than reported values for Gd166 ($\mathcal{J}^{\text{MG}} = 2$ meV) and Tb166 ($\mathcal{J}^{\text{MT}} = 1.8$ meV) which is consistent with the expected trend.

Mn easy-plane anisotropy. Mn has an easy-plane (planar) anisotropy with $K^{\text{M}} > 0$. The magnitude of K^{M} in R166 compounds has been estimated to be in a range from 0.2 to 0.5 meV from a variety of experimental approaches; (1) fitting the spin gap of Tb166 results in $K^{\text{M}} = 0.44$ meV [2]; (2) reported from analysis of the magnetization data as 0.47 meV for Tb166 [4] (3) reported to be 0.23 meV from the $\mathbf{H} \parallel \mathbf{c}$ saturation magnetization field of Gd166 [5]; (4) reported as 0.2 meV for Y166 [6].

For Er166, the best estimate of K^{M} is obtained from the high-temperature magnetization data with $\mathbf{H} \parallel \mathbf{c}$, as shown in Fig. 7a of the main text. At temperatures where the Er MAE is quenched ($T \sim 200$ K), the critical field for ferrimagnetic alignment of Mn and Er moments is approximately $\mu_0 H_c = 5$ T. If this critical field is determined solely by the MAE of the Mn ion, we estimate that $K^{\text{M}} \approx \mu_0 H_c/12M = 0.17$ meV,

where $M = 7\ \mu_B$ is the onset of the magnetization plateau at 200 K. This value of K^{M} is on the low end of the range of the other $R166$ compounds and so we fix $K^{\mathrm{M}} = 0.17$ meV.

Er crystalline-electric-field parameters. The crystalline-electric-field (CEF) parameters B_l^m for different rare-earth ions scale according to the formula

$$B_l^m = \langle r^l \rangle \theta_l A_l^m \tag{1}$$

where θ_l is the Steven's factor and $\langle r^l \rangle$ is the average l^{th} order radial moment, both of which depend on the R ion. The parameter A_l^m is intrinsic to the crystalline potential and is expected to vary slowly across the $R166$ series.

From INS studies of Tb166, we are able to determine approximate values of $A_2^0 = (4.1\ \mathrm{meV})a_0^{-2}$, $A_4^0 = -(7.0\ \mathrm{meV})a_0^{-4}$, and $A_6^0 \approx 0$ (where a_0 is the Bohr radius). Assuming the transferability of the CEF potential for the hexagonal $R166$s and using Eq. (1), we obtain good starting values for the CEF parameters for the Er ion; $B_2^0 = 0.0075$ meV, $B_4^0 = -0.00041$ meV and $B_6^0 = 0$. These values are reasonably consistent with DFT studies of the $R\mathrm{Mn_6Sn_6}$ series [3] and slight refinement of these values are described below. For Er166, magnetization measurements indicate an easy-axis along the $(1, 1, 0)$ direction in the hexagonal unit cell (see Ref. [7]) implying that the in-plane anisotropy term B_6^6 is positive ($B_6^6 > 0$).

Global search. Next we describe estimates of B_l^m and $\mathcal{J}^{\mathrm{ME}}$ for Er166 from comparison of magnetization and INS data. In this search, we fix the other parameters of the model (i.e. $\mathcal{J}_i^{\mathrm{MM}}$ and K^{M}). Supplementary Figure 4 shows data from INS measurements of Er166 where we observe four CEF excitations out of the ground state at $T = 5$ K. These excitations are not visible at 200 K due to thermal depopulation of the ground state. The energies of the first four transitions were obtained from gaussian fits to the peaks and are listed in Table 2.

As shown in Fig. 7a of the main text, an applied magnetic field along the hard $(0, 0, 1)$ direction will generate a first-order magnetization process (FOMP) where the ground-state FIM structure jumps from spins ordered with their orientations in the ab-plane (planar) to their orientations lying along the c-axis (uniaxial). The small value of the critical FOMP field [$\mu_0 H_{\mathrm{c}} = 0.7(2)$ T] indicates that the planar and uniaxial configurations are nearly degenerate with a free energy difference of $\Delta\mathcal{F} = \mathcal{F}_{\mathrm{c}} - \mathcal{F}_{\mathrm{ab}} \approx M\mu_0 H_{\mathrm{c}} = 0.16(5)$ meV, where $M = 4\ \mu_B$/fu is the net magnetization per formula unit in the FIM ground state.

We can use a combination of INS and magnetization data to refine our estimates of these parameters. Supplementary Figure 5 shows a representative slice of a search in the 4-D space of B_l^m and $\mathcal{J}^{\mathrm{ME}}$ parameters. The indicated regions for the different observables correspond to the values in Table 2. In Supplementary Figure 5, the selected parameters are indicated by the red dot and provide good estimates of $\Delta\mathcal{F}$, E_1, and E_3, whereas agreement with E_2 and E_4 is less optimal. The black curve in Supplementary Figure 4 compares the calculated CEF transitions from this parameter set to the INS data. The main text demonstrates that our model with these parameters displays reasonable agreement with the observed data and is valuable in interpreting experimental results.

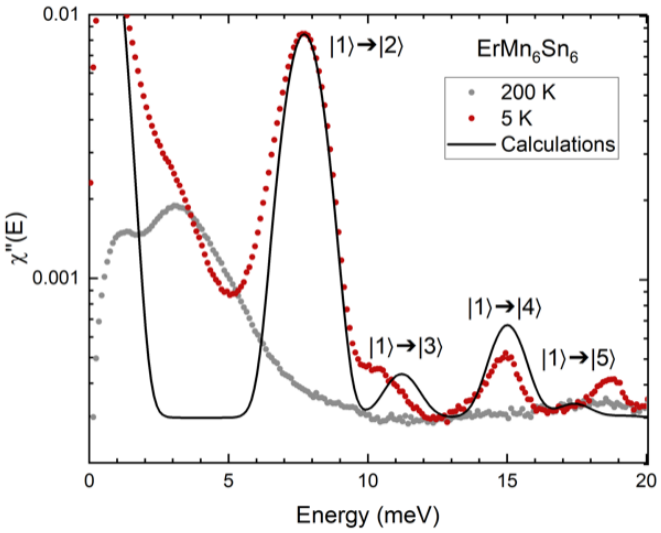

Supplementary Figure 4 Comparison of inelastic-neutron-scattering (INS) data at $T = 5$ K and 200 K to calculations of the trace of the imaginary part of the local-ion magnetic susceptibility (black line) using the parameters determined in Supplementary Figure 5. INS data were measured on the ARCS spectrometer at the Spallation Neutron Source using an incident energy of 30 meV. Data are summed over $h = 0.25$ to 0.75, $k = -0.25$ to 0.25, and $l = -5$ to 5 for the hexagonal reciprocal lattice.

Supplementary Table 2 Energies obtained from magnetization data [$\Delta\mathcal{F}$(FOMP)] and crystalline-electric-field (CEF) transitions (Ei) seen in inelastic-neutron-scattering data. These energies are used to determine the Hamiltonian parameters for Er166. The numbers for the CEF states are general labels starting from the ground state $|1\rangle$.

Observable	Energy (meV)
$\Delta\mathcal{F}$ (FOMP)	0.16(5)
$E1(\|1\rangle \rightarrow \|2\rangle)$	7.65(1)
$E2(\|1\rangle \rightarrow \|3\rangle)$	10.50(15)
$E3(\|1\rangle \rightarrow \|4\rangle)$	14.85(13)
$E4(\|1\rangle \rightarrow \|5\rangle)$	18.6(3)

1.5 Classical magnetic anisotropy energy

The classical magnetic anisotropy energy (MAE) for hexagonal Er166 is given by

$$K_{\rm tot} = K_1 \sin^2\theta_{\rm Er} + K_2 \sin^4\theta_{\rm Er} + K_3 \sin^6\theta_{\rm Er} + K_3' \cos(6\varphi_{\rm Er}) \sin^6\theta_{\rm Er} - 6K^{\rm M} \sin^2\theta_{\rm Mn}. \quad (2)$$

where θ_i and φ_i are the polar and azimuthal angles, respectively, describing the orientation of the Er ($i = $ Er) and Mn ($i = $ Mn) magnetic moments. For Mn, we retain only the first-order MAE term and for Er we assume that $K_3 = 0$. The MAE constants for Er are related to the B_l^m parameters, $K_1 = -3J^{(2)}B_2^0 - 40J^{(4)}B_4^0$, $K_2 = 35J^{(4)}B_4^0$,

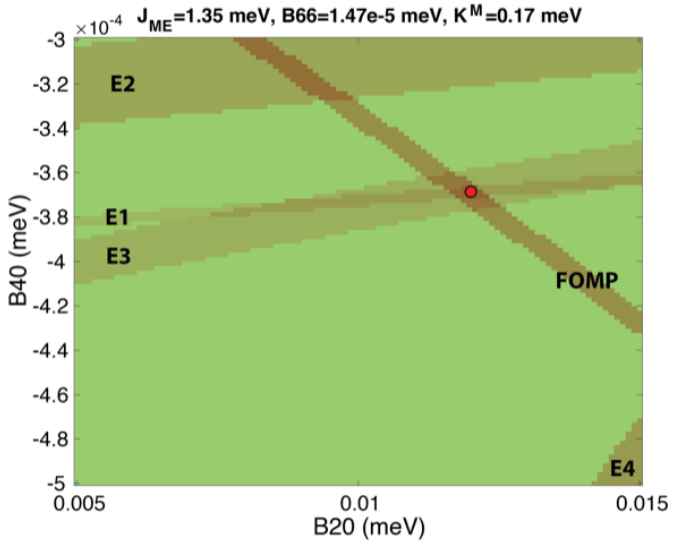

Supplementary Figure 5 Global search for model parameters as a function of B_2^0 and B_4^0 for fixed values of $\mathcal{J}^{\rm ME} = 1.35$ meV, $B_6^6 = 1.47 \times 10^{-5}$ meV, and $K^{\rm M} = 0.17$ meV, and all other exchange constants fixed as described in the text. Striped regions correspond to observables listed in Table 2. The red dot shows a choice of parameters for B_2^0 and B_4^0 that best represents the first-order magnetization process (FOMP) and the $E1$, and E_3 crystalline-electric-field transitions.

and $K_3' = J^{(6)} B_6^6$, where $J^{(2)} = J(J-1/2)$, $J^{(4)} = J^{(2)}(J-1)(J-3/2)$, and $J^{(6)} = J^{(4)}(J-2)(J-5/2)$.

We find that $K_{\rm tot} = 0$ for a uniaxial ferrimagnet (FIM-c) with $\theta_{\rm Er} = \pi$ and $\theta_{\rm Mn} = 0$ and $K_{\rm tot} = K_1 + K_2 - K_3' - 6K^{\rm M} < 0$ for a planar ferrimagnet (FIM-ab) with the in-plane easy-axis defined by $\theta_{\rm Er} = \theta_{\rm Mn} = \pi/2$ and $\varphi_{\rm Er} = \pi/6$. Using our Er CEF parameters, we obtain $K_1 = 28.34$, $K_2 = -26.45$, $K_3' = 0.83$, and $6K^{\rm M} = 1.02$ meV. The classical polar and planar MAE are plotted in Supplementary Figures 6a and 6b, respectively, and demonstrate the near degeneracy of uniaxial and planar configurations which arise from an almost complete cancellation of Mn and Er MAE contributions. We find that the classical MAE slightly favors the FIM-c phase ($K_{\rm tot} = 0.04$ meV), whereas experimentally FIM-ab is the ground state and we estimate $K_{\rm tot} \approx -M\mu_0 H_{\rm FOMP}/2 = -0.08$ meV from the FOMP field, as described above.

Evaluation of the MAE using a mean-field approach does establish the FIM-ab state as the ground state. Furthermore, orbital mixing of the CEF eigenstates reduces $\mu_{\rm Er}$ and leads to differences between the classical and mean-field results. This is illustrated by the small differences between the classical and mean-field curves shown in Fig. 6a for a progressively tilted collinear-FIM structure with $\theta_{\rm Mn} = \theta$ and $\theta_{\rm Er} = \pi - \theta$ at $T = 0$ K. Similarly, Supplementary Figure 6b compares the classical and free-energy results for the Er six-fold planar MAE, demonstrating that the easy axis is rotated 30° away from **a**. Note that the CEF level mixing captured in the mean-field approach leads to a sizable reduction of the planar MAE due to its dependence on the sixth-order matrix elements of the angular-momentum operators.

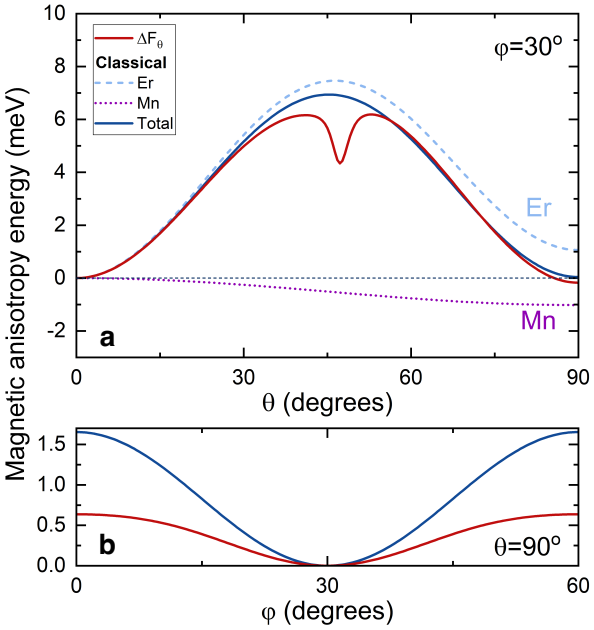

Supplementary Figure 6 Ground state magnetic anisotropy energy (MAE) of $ErMn_6Sn_6$ as a function of **a** the polar angle (θ) and **b** the planar angle (φ) in both the classical limit (blue) and from free energy calculations (red). In **a**, the separate contributions of Er (blue dash) and Mn (purple dot) to the classical MAE are shown.

1.6 Mean-field description of the free energy

The typical mean-field decomposition of the exchange Hamiltonian Eq. (1) of the main text is given by,

$$\begin{aligned}\mathcal{H}_{\text{ex}}^{\text{MF}} =& \mathcal{J}^{\text{ME}} \sum_{\langle i<j \rangle} \left(\langle \mathbf{s}_i \rangle \cdot \mathbf{S}_j + \mathbf{s}_i \cdot \langle \mathbf{S}_j \rangle - \langle \mathbf{s}_i \rangle \cdot \langle \mathbf{S}_j \rangle \right) \\ &+ \sum_{i,j} \mathcal{J}_{ij}^{\text{MM}} \left(\langle \mathbf{s}_i \rangle \cdot \mathbf{s}_j + \mathbf{s}_i \cdot \langle \mathbf{s}_j \rangle - \langle \mathbf{s}_i \rangle \cdot \langle \mathbf{s}_j \rangle \right). \end{aligned} \tag{3}$$

We use these terms to generate local mean-field Hamiltonians for Er and Mn

$$\mathcal{H}_{\text{Er}}^{\text{MF}} = \mathcal{H}_{\text{Er}} - \mathbf{B}_{\text{Er}} \cdot \mathbf{S} - g_J \mu_{\text{B}} \mathbf{J} \cdot \mu_0 \mathbf{H} \tag{4}$$

and

$$\mathcal{H}_{\text{Mn}}^{\text{MF}} = \mathcal{H}_{\text{Mn}} - \mathbf{B}_{\text{Mn}} \cdot \mathbf{s} - g \mu_{\text{B}} \mathbf{s} \cdot \mu_0 \mathbf{H}\,, \tag{5}$$

where $\mathbf{B}_{\text{Mn}} = -2\mathcal{J}^{\text{ME}} \langle \mathbf{S} \rangle - \sum_i \gamma_i \mathcal{J}_i^{\text{MM}} \langle \mathbf{s}_i \rangle$ and $\mathbf{B}_{\text{Er}} = -12\mathcal{J}^{\text{ME}} \langle \mathbf{s} \rangle$ are the self-consistently determined molecular fields acting on Mn and Er, respectively. γ_i is the coordination number for $\mathcal{J}_i^{\text{MM}}$.

The self-consistent solution to the mean-field Hamiltonian is obtained by minimizing the free energy

$$\begin{aligned}\mathcal{F}(T, H_z) = &-k_B T \ln Z_{\mathrm{Er}} - 6 k_B T \ln Z_{\mathrm{Mn}} \\ &- 12 \mathcal{J}^{\mathrm{ME}} \langle \mathbf{s} \rangle \cdot \langle \mathbf{S} \rangle - 3 \sum_i \gamma_i \mathcal{J}_i^{\mathrm{MM}} \langle \mathbf{s}_i \rangle \cdot \langle \mathbf{s} \rangle \ ,\end{aligned} \tag{6}$$

where Z_{Er} and Z_{Mn} are the partition functions for Er and Mn obtained from Eqs. (4) and (5), respectively.

To simplify our analysis, we consider only uniaxial fields $\mathbf{H} \parallel \mathbf{c}$ (i.e. H_z) and make an approximation where the planar Er magnetic-anisotropy energy (MAE) given by $K_3' \sin^6 \theta_{\mathrm{Er}} \cos(6\varphi_{\mathrm{Er}})$ (where $K_3' \propto B_6^6$) is fixed at its minimum value of $-K_3' \sin^6 \theta_{\mathrm{Er}}$ for any in-plane angle φ_{Er}. This is equivalent to an easy-plane anisotropy with nonzero B_6^0, as the θ dependence plays a critical role in controlling the phase stability. Furthermore, Fig. 6a in the main text shows that the true easy-plane limit ($K_3' \approx 0$) is valid at high temperatures ($T > 100$ K) due to rapid thermal softening of the planar MAE upon warming. This approximation effectively describes the low-temperature magnetic phases, such as FIM, where all moments lie in a vertical plane containing the planar easy-axis and c-axis field directions.

Zero-field case. For easy-plane configurations [$K_3' \cos(6\varphi_{\mathrm{Er}}) = const.$] in zero field, only the relative angles between spins matter. In the specific case of the ideal-triple-spiral structure, the periodicity is defined by the angle Φ between alike layers in adjacent cells (coupled by $\mathcal{J}_3^{\mathrm{MM}}$) and the angle δ is between strongly coupled Mn bilayers (coupled by $\mathcal{J}_2^{\mathrm{MM}}$). Supplementary Figure 7 (and Fig. 1 of the main text) shows the relative angles of spins in neighboring layers and their coupling constants. In Supplementary Figure 7, the Er moment is arbitrarily chosen to point along $(\bar{1}, 0, 0)$, bisecting the angle $(\Phi - \delta)$ and the Mn moment directions. The Mn moments are specified by layer designations A, B, A+, A-, and B- and their orientations are given relative to the Er moment orientation. The spin vectors are

$$\begin{aligned}\mathbf{S} &= S(\bar{1}, 0, 0) \, , \\ \mathbf{s}_{\mathrm{A}} &= s \left[\cos\left(\frac{\Phi - \delta}{2}\right), -\sin\left(\frac{\Phi - \delta}{2}\right), 0 \right] \, , \\ \mathbf{s}_{\mathrm{B}} &= s \left[\cos\left(\frac{\Phi - \delta}{2}\right), \sin\left(\frac{\Phi - \delta}{2}\right), 0 \right] \, , \\ \mathbf{s}_{\mathrm{A\text{-}}} &= s \left[\cos\left(\frac{3\Phi - \delta}{2}\right), -\sin\left(\frac{3\Phi - \delta}{2}\right), 0 \right] \, , \\ \mathbf{s}_{\mathrm{A+}} &= s \left[\cos\left(\frac{\Phi + \delta}{2}\right), \sin\left(\frac{\Phi + \delta}{2}\right), 0 \right] \, , \\ \mathbf{s}_{\mathrm{B\text{-}}} &= s \left[\cos\left(\frac{\Phi + \delta}{2}\right), -\sin\left(\frac{\Phi + \delta}{2}\right), 0 \right] \, ,\end{aligned} \tag{7}$$

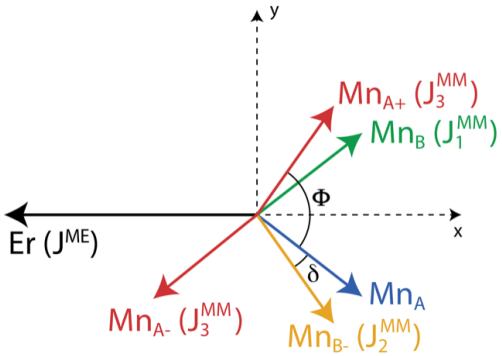

Supplementary Figure 7 Geometry of spins in neighboring layers in the easy-plane triple-spiral state. We place the Er spin (black) arbitrarily along the $(\bar{1}, 0, 0)$ direction and it's molecular field is determined by the $\mathcal{J}^{\mathrm{ME}}$ coupling to the $\mathrm{Mn_A}$ (blue) and $\mathrm{Mn_B}$ (green) in the layers above and below. The blue $\mathrm{Mn_A}$ spin experiences a molecular field from the $\mathrm{Mn_{A+}}$ and $\mathrm{Mn_{A-}}$ (red), $\mathrm{Mn_{B-}}$ (yellow), $\mathrm{Mn_B}$ (green) and the Er spin with the exchange parameters indicated in parentheses.

and Supplementary Figure 7 shows the relative angles of spins in neighboring layers and their coupling constants.

In the zero-field case, expressions for the molecular fields are

$$\begin{aligned}\mathbf{B}_{\mathrm{Er}} &= -6\mathcal{J}^{\mathrm{ME}}\left(\langle \mathbf{s}_{\mathrm{A}}\rangle + \langle \mathbf{s}_{\mathrm{B}}\rangle\right), \\ &= -12\mathcal{J}^{\mathrm{ME}}\langle s\rangle \cos\left(\frac{\Phi-\delta}{2}\right)(1,0,0),\end{aligned} \tag{8}$$

and

$$\begin{aligned}\mathbf{B}_{\mathrm{Mn}} &= -2\mathcal{J}^{\mathrm{ME}}\langle \mathbf{S}\rangle - 4\mathcal{J}_0^{\mathrm{MM}}\langle \mathbf{s}_{\mathrm{A}}\rangle - \mathcal{J}_1^{\mathrm{MM}}\langle \mathbf{s}_{\mathrm{B}}\rangle \\ &- \mathcal{J}_2^{\mathrm{MM}}\langle \mathbf{s}_{\mathrm{B\text{-}}}\rangle - \mathcal{J}_3^{\mathrm{MM}}\left(\langle \mathbf{s}_{\mathrm{A+}}\rangle + \langle \mathbf{s}_{\mathrm{A\text{-}}}\rangle\right), \\ &= 2\mathcal{J}^{\mathrm{ME}}\langle S\rangle(1,0,0) \\ &- \left(4\mathcal{J}_0^{\mathrm{MM}} + 2\mathcal{J}_3^{\mathrm{MM}}\cos\Phi\right)\langle s\rangle \\ &\times \left[\cos\left(\frac{\Phi-\delta}{2}\right), -\sin\left(\frac{\Phi-\delta}{2}\right), 0\right] \\ &- \mathcal{J}_1^{\mathrm{MM}}\langle s\rangle\left[\cos\left(\frac{\Phi-\delta}{2}\right), \sin\left(\frac{\Phi-\delta}{2}\right), 0\right] \\ &- \mathcal{J}_2^{\mathrm{MM}}\langle s\rangle\left[\cos\left(\frac{\Phi+\delta}{2}\right), -\sin\left(\frac{\Phi+\delta}{2}\right), 0\right].\end{aligned} \tag{9}$$

The resulting free energy per unit cell is given by

$$\begin{aligned}\mathcal{F} &= -k_B T \ln Z_{\mathrm{Er}} - 6k_B T \ln Z_{\mathrm{Mn}} \\ &+ 12\mathcal{J}^{\mathrm{ME}}\langle s\rangle\langle S\rangle \cos\left(\frac{\Phi-\delta}{2}\right)\end{aligned} \tag{10}$$

$$
\begin{aligned}
&- 3\langle s\rangle^2 \left[4\mathcal{J}_0^{\mathrm{MM}} + \mathcal{J}_1^{\mathrm{MM}}\cos(\Phi-\delta) + \mathcal{J}_2^{\mathrm{MM}}\cos\delta\right. \\
&\left.+2\mathcal{J}_3^{\mathrm{MM}}\cos\Phi\right] ,
\end{aligned}
$$

where the thermally averaged spin magnitudes $\langle s\rangle$ and $\langle S\rangle$ are determined self-consistently.

Vertical-field case. For a vertical magnetic field along the **z** (i.e. **c**) direction, we maintain the double spiral angles δ and Φ and now introduce the polar angles of the Er and Mn sublattices θ_{Er} and θ_{Mn}. Similar to the definitions above, we assume that the Er moment is pointed in the $(1,0,1)$ plane and always negative in the $x-$direction. The spin vectors are

$$
\begin{aligned}
\mathbf{S} &= S\left[-\sin\theta_{\mathrm{Er}}, 0, \cos\theta_{\mathrm{Er}}\right] , \\
\mathbf{s}_{\mathrm{A}} &= s\left[\sin\theta_{\mathrm{Mn}}\cos\left(\frac{\Phi-\delta}{2}\right), -\sin\theta_{\mathrm{Mn}}\sin\left(\frac{\Phi-\delta}{2}\right), \cos\theta_{\mathrm{Mn}}\right] , \\
\mathbf{s}_{\mathrm{B}} &= s\left[\sin\theta_{\mathrm{Mn}}\cos\left(\frac{\Phi-\delta}{2}\right), \sin\theta_{\mathrm{Mn}}\sin\left(\frac{\Phi-\delta}{2}\right), \cos\theta_{\mathrm{Mn}}\right] , \\
\mathbf{s}_{\mathrm{A}\text{-}} &= s\left[\sin\theta_{\mathrm{Mn}}\cos\left(\frac{3\Phi-\delta}{2}\right), -\sin\theta_{\mathrm{Mn}}\sin\left(\frac{3\Phi-\delta}{2}\right), \cos\theta_{\mathrm{Mn}}\right] , \\
\mathbf{s}_{\mathrm{A}+} &= s\left[\sin\theta_{\mathrm{Mn}}\cos\left(\frac{\Phi+\delta}{2}\right), \sin\theta_{\mathrm{Mn}}\sin\left(\frac{\Phi+\delta}{2}\right), \cos\theta_{\mathrm{Mn}}\right] , \\
\mathbf{s}_{\mathrm{B}\text{-}} &= s\left[\sin\theta_{\mathrm{Mn}}\cos\left(\frac{\Phi+\delta}{2}\right), -\sin\theta_{\mathrm{Mn}}\sin\left(\frac{\Phi+\delta}{2}\right), \cos\theta_{\mathrm{Mn}}\right] .
\end{aligned} \tag{11}
$$

The corresponding molecular fields are given by similar expressions as above and include an externally applied magnetic field along the $z-$axis.

$$
\begin{aligned}
\mathbf{B}_{\mathrm{Er}} &= -12\mathcal{J}^{\mathrm{ME}}\langle s\rangle\left[\sin\theta_{\mathrm{Mn}}\cos\left(\frac{\Phi-\delta}{2}\right), 0, \cos\theta_{\mathrm{Mn}}\right] \\
&\quad +\mu_0 H_z(0,0,1) , \\
\mathbf{B}_{\mathrm{Mn}} &= -2\mathcal{J}^{\mathrm{ME}}\langle S\rangle[-\sin\theta_{\mathrm{Er}}, 0, \cos\theta_{\mathrm{Er}}] \\
&\quad -4\mathcal{J}_0^{\mathrm{MM}}\langle s\rangle \\
&\quad \times\left[\sin\theta_{\mathrm{Mn}}\cos\left(\frac{\Phi-\delta}{2}\right), -\sin\theta_{\mathrm{Mn}}\sin\left(\frac{\Phi-\delta}{2}\right), \cos\theta_{\mathrm{Mn}}\right] \\
&\quad -\mathcal{J}_1^{\mathrm{MM}}\langle s\rangle \\
&\quad \times\left[\sin\theta_{\mathrm{Mn}}\cos\left(\frac{\Phi-\delta}{2}\right), \sin\theta_{\mathrm{Mn}}\sin\left(\frac{\Phi-\delta}{2}\right), \cos\theta_{\mathrm{Mn}}\right] \\
&\quad -\mathcal{J}_2^{\mathrm{MM}}\langle s\rangle \\
&\quad \times\left[\sin\theta_{\mathrm{Mn}}\cos\left(\frac{\Phi+\delta}{2}\right), -\sin\theta_{\mathrm{Mn}}\sin\left(\frac{\Phi+\delta}{2}\right), \cos\theta_{\mathrm{Mn}}\right]
\end{aligned} \tag{12}
$$

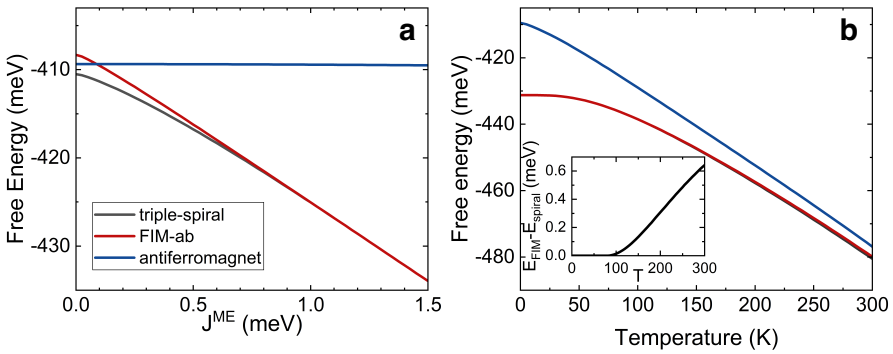

Supplementary Figure 8 Free energies of the zero-field magnetic phases in $ErMn_6Sn_6$. We calculate the phase stability of different planar ($\theta_{\rm Er} = \theta_{\rm Mn} = \pi/2$) ferrimagnetic (FIM-ab), antiferromagnetic, and spiral phases using a mean-field analysis of the easy-plane model for $ErMn_6Sn_6$. **a** Free energy of different planar magnetic ground states at $T = 0$ K as a function of $\mathcal{J}^{\rm ME}$. **b** The temperature dependence of the phase stability of the planar states with $\mathcal{J}^{\rm ME} = 1.35$ meV. The inset to **b** shows the small free energy difference between the FIM-ab and triple-spiral phases.

$$
\begin{aligned}
&-2\mathcal{J}_3^{\rm MM}\langle s\rangle \left[\sin\theta_{\rm Mn}\cos\Phi\cos\left(\frac{\Phi-\delta}{2}\right), \ldots\right.\\
&\left.\ldots -\sin\theta_{\rm Mn}\cos\Phi\sin\left(\frac{\Phi-\delta}{2}\right), \cos\theta_{\rm Mn}\right]\\
&+\mu_0 H_z(0,0,1)\,. \qquad (13)
\end{aligned}
$$

Using the same notation, the free energy is

$$
\begin{aligned}
\mathcal{F} = &-k_B T\ln Z_{\rm Er} - 6k_B T\ln Z_{\rm Mn} \qquad (14)\\
&+12\mathcal{J}_0^{\rm MM}\langle s\rangle^2 + 12\mathcal{J}^{\rm ME}\langle S\rangle\langle s\rangle\\
&\times\left[-\sin\theta_{\rm Mn}\sin\theta_{\rm Er}\cos\left(\frac{\Phi-\delta}{2}\right)+\cos\theta_{\rm Mn}\cos\theta_{\rm Er}\right]\\
&+3\mathcal{J}_1^{\rm MM}\langle s\rangle^2\left[\sin^2\theta_{\rm Mn}\cos(\Phi-\delta)+\cos^2\theta_{\rm Mn}\right]\\
&+3\mathcal{J}_2^{\rm MM}\langle s\rangle^2\left(\sin^2\theta_{\rm Mn}\cos\delta+\cos^2\theta_{\rm Mn}\right)\\
&+6\mathcal{J}_3^{\rm MM}\langle s\rangle^2\left(\sin^2\theta_{\rm Mn}\cos\Phi+\cos^2\theta_{\rm Mn}\right)\,.
\end{aligned}
$$

Supplementary Figure 9 shows the evolution of the polar angles and total magnetization that result from minimization of the free energy for $T = 0$ and $T = 125$ K as a function of applied field. Similar calculations were used to assemble the phase diagram shown in Fig. 8 of the main text.

Classical energy states with planar anisotropy. States with non-zero planar anisotropy or under in-plane magnetic fields can adopt distorted magnetic structures. The moment directions can vary in a complex manner from layer-to-layer within a large magnetic unit cell determined by the overall periodicity. Rather than attempt to evaluate the self-consistent solutions to the free energy, where molecular fields must be evaluated independently for each layer, we rather minimize the total energy of the

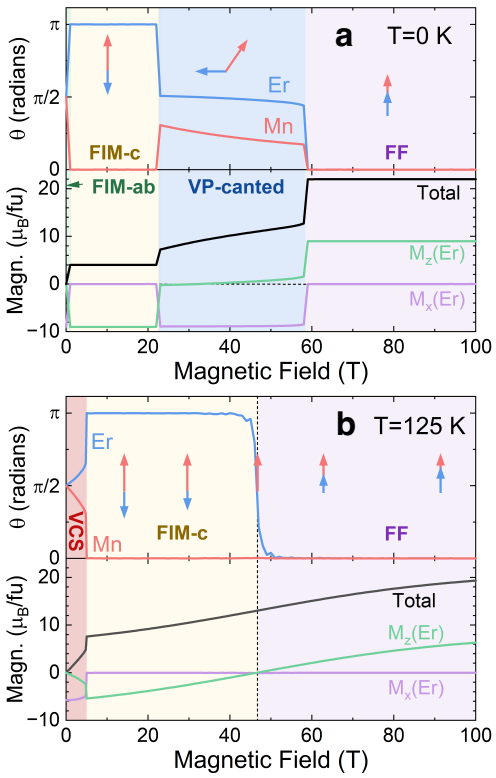

Supplementary Figure 9 Evolution of different magnetic phases obtained from the minimization of the free energy. Plots show the polar angles and total magnetization as a function of $\mathbf{H} \parallel \mathbf{c}$ for **a** $T = 0$ K and **b** $T = 125$ K.

form

$$
\begin{aligned}
E = \sum_{j=1}^{p} \big(& 3\mathcal{J}_1^{\mathrm{MM}} s^2 \cos\left(\phi_{2j-1} - \phi_{2j}\right) \\
& + 3\mathcal{J}_2^{\mathrm{MM}} s^2 \cos\left(\phi_{2j} - \phi_{2j+1}\right) \\
& + 3\mathcal{J}_3^{\mathrm{MM}} s^2 \left[\cos\left(\phi_{2j-1} - \phi_{2j+1}\right) + \cos\left(\phi_{2j} - \phi_{2j+2}\right)\right] \\
& + 6\mathcal{J}^{\mathrm{ME}} sS \left[\cos\left(\phi_{2p+j} - \phi_{2j-1}\right) + \cos\left(\phi_{2p+j} - \phi_{2j}\right)\right] \\
& + K_3' \cos\left(6\phi_{2p+j}\right) \\
& - \mu_B \mu_0 H_x \left\{3gs\left[\cos\left(\phi_{2j-1}\right) + \cos\left(\phi_{2j}\right)\right] + g_J J \cos\left(\phi_{2p+j}\right)\right\} \\
& - \mu_B \mu_0 H_y \left\{3gs\left[\sin\left(\phi_{2j-1}\right) + \sin\left(\phi_{2j}\right)\right] + g_J J \sin\left(\phi_{2p+j}\right)\right\} \big) \, .
\end{aligned}
\tag{15}
$$

Here, p is the number of unit cells containing an Mn-Er-Mn trilayer and j labels a single unit cell. Mn and Er moments adopt a planar angle ϕ_i in each successive layer in the stack with $i = 1$ to $2p$ and $i = 2p + 1$ to $3p$, respectively, with open boundary conditions. We find the minimum energy using the exchange parameters in Table 1 of

the main text and for different values of the in-plane anisotropy parameter K_3'. The mean periodicity is shown in Fig. 6b of the main text for a stack consisting of $p = 36$ unit cells (108 layers).

References

[1] Riberolles, S. X. M. *et al.* Low-Temperature Competing Magnetic Energy Scales in the Topological Ferrimagnet $TbMn_6Sn_6$. *Phys. Rev. X* **12**, 021043 (2022). URL https://link.aps.org/doi/10.1103/PhysRevX.12.021043.

[2] Riberolles, S. X. M. *et al.* Orbital character of the spin-reorientation transition in $TbMn_6Sn_6$. *Nat. Commun.* **14**, 2658 (2023). URL https://doi.org/10.1038/s41467-023-38174-5.

[3] Lee, Y. *et al.* Interplay between magnetism and band topology in the kagome magnets RMn_6Sn_6. *Phys. Rev. B* **108**, 045132 (2023). URL https://link.aps.org/doi/10.1103/PhysRevB.108.045132.

[4] Jones, D. C. *et al.* Origin of spin reorientation and intrinsic anomalous Hall effect in the kagome ferrimagnet $TbMn_6Sn_6$ (2022). URL https://arxiv.org/abs/2203.17246. 2203.17246.

[5] Rosenfeld, E. V. & Mushnikov, N. V. Double-flat-spiral magnetic structures: Theory and application to the RMn_6X_6 compounds. *Phys. B: Condens. Matter* **403**, 1898–1906 (2008). URL https://www.sciencedirect.com/science/article/pii/S0921452607012690.

[6] Ghimire, N. J. *et al.* Competing magnetic phases and fluctuation-driven scalar spin chirality in the kagome metal YMn_6Sn_6. *Sci. Adv.* **6**, eabe2680 (2020). URL https://www.science.org/doi/abs/10.1126/sciadv.abe2680.

[7] Suga, K. *et al.* High-field-magnetization study of an $ErMn_6Sn_6$ single crystal. *J. Alloys Compd.* **408-412**, 158–160 (2006). URL https://www.sciencedirect.com/science/article/pii/S092583880500589X.